$Ba_2NaNb_5O_{15}$ single crystals doped with Tm^{3+} and Ho^{3+}: spectroscopy and energy transfer parameters

2007 J. Phys.: Condens. Matter 19 476208

(http://iopscience.iop.org/0953-8984/19/47/476208)

IOP PUBLISHING JOURNAL OF PHYSICS: CONDENSED MATTER

J. Phys.: Condens. Matter **19** (2007) 476208 (11pp) doi:10.1088/0953-8984/19/47/476208

$Ba_2NaNb_5O_{15}$ single crystals doped with Tm^{3+} and Ho^{3+}: spectroscopy and energy transfer parameters

S Bigotta[1], M Tonelli[1] and E Cavalli[2]

[1] NEST, Dipartimento di Fisica, Università di Pisa, largo Pontecorvo 3, 56127 Pisa, Italy
[2] Dipartimento di Chimica Generale ed Inorganica, Chimica Analitica e Chimica Fisica, Università di Parma, Via G P Usberti 17/a, 43100 Parma, Italy

E-mail: bigotta@df.unipi.it

Received 23 April 2007, in final form 27 August 2007
Published 31 October 2007
Online at stacks.iop.org/JPhysCM/19/476208

Abstract

Single crystals of $Ba_2NaNb_5O_{15}$ (BNN) activated with Ho^{3+} and Tm^{3+} have been grown by the 'flux growth' technique. The absorption spectra, the visible emission properties and the decay curves of the excited states have been measured at 10 and 298 K. The room temperature absorption spectra have been analysed by means of the Judd–Ofelt theory and the intensity parameters have been evaluated. The spontaneous transition probabilities, the branching ratios and the radiative lifetimes of the excited states have been calculated and compared with the experimental data in order to estimate the efficiency of the non-radiative processes. The connection between structural and spectroscopic properties has been pointed out in relation to the possible applications of these materials.

1. Introduction

In this work we explore the optical properties of $Ba_2NaNb_5O_{15}$ (hereafter referred to as BNN) crystals doped with Tm^{3+} or Ho^{3+} ions in order to investigate and subsequently develop new widely tunable solid-state laser sources operating at around 2 μm. The laser devices emitting in this wavelength range are of great interest for atmospheric and space applications, including coherent Doppler velocimetry and gas detection, atmospheric wind sensors for full-scale earth observation satellites, metrology, optical communications, detection of pollutants and coherent laser radars, medical surgery, etc [1]. The most suitable 2 μm laser channels are $^3F_4 \rightarrow {}^3H_6$ (Tm^{3+}) and $^5I_7 \rightarrow {}^5I_8$ (Ho^{3+}) [2], the latter having better characteristics in terms of emission cross section and longer wavelength [3]. On the other hand it is well known that Ho^{3+} based materials can be conveniently co-doped with Tm^{3+} in order to obtain efficient 2 μm laser media suitable for diode pumping [4]. In previous papers we have demonstrated that in BNN the $Tm^{3+} \rightarrow Ho^{3+}$ energy transfer process is particularly efficient [5] and that this host lattice has attractive potentialities in solid-state laser technology [6, 7]. In this connection it is important to have a detailed knowledge of the spectral properties of Tm^{3+} and Ho^{3+} singly doped BNN

crystals. We have, therefore, grown these crystals and measured their 10 (LT) and 298 K (RT) absorption and emission spectra and their fluorescence dynamics. From the oscillator strengths of the absorption transitions, the Judd–Ofelt intensity parameters have been evaluated. The spontaneous transition probabilities, the branching ratios and the radiative lifetimes have been determined for the most important emitting states using the calculated intensity parameters and the results have been compared with the experimental data in order to estimate the efficiency of the non-radiative processes in these materials.

2. Experimental setup

The crystals were grown by means of the flux growth method. Pure BaO, Nb_2O_5 and $Na_2B_4O_7$ were used as starting materials. The activator ions were added as Ho_2O_3 and Tm_2O_3. We have grown singly doped crystals with 1 and 14% Ho/Ba and 1 and 10.5% Tm/Ba nominal molar ratios, and co-doped crystals with Ho/Ba = 0.7% and Tm/Ba = 7%. The starting mixture was put in a Pt crucible and heated to melt (1250 °C) in a horizontal furnace. After a 12 h soaking time, the temperature was slowly lowered (2–3 °C h^{-1}) to 400 °C, then the furnace was turned off. Crystals with maximum size of $2 \times 2 \times 3$ mm^3 and good optical quality were separated from the flux by dissolving it in hot diluted HCl. The absorption and emission spectra of the singly doped crystals were measured using the concentrated samples. Their actual concentrations were determined by x-ray fluorescence analysis, yielding segregation coefficients of 0.53 for Ho^{3+} and of 0.33 for Tm^{3+}. The fluorescence lifetimes of the singly doped and co-doped crystals have been measured as a function of the temperature using diluted crystals in order to exclude as much as possible cooperative and clustering effects.

The samples were optically polished and mounted onto the cold finger of a He-closed cycle cryostat. The 10 (LT) and 298 K (RT) polarized absorption spectra were measured with a spectroscopic system equipped with a 300 W halogen lamp fitted with a 0.25 m monochromator as source and a 1.26 m monochromator with an RCA C31034 photomultiplier or a PbS cell to read and detect the output radiation. The visible and infrared emission spectra were measured at 10 and 298 K by exciting the sample using an Ar^+ ion laser or a laser diode. The emission was mechanically chopped and focused by a lens on the input slit of a 0.25 m monochromator and detected by a photomultiplier with S-20 spectral response (visible) or a cooled InSb detector (near infrared (NIR)). The signal was processed by a lock-in amplifier and the optical response of the system was normalized for both polarizations by use of a black-body source at 3000 K temperature. The resolution was 0.1 nm in the visible and 1 nm in the NIR. For the lifetime measurements the setup was similar, but the sample was pumped by either a 10 Hz pulsed Ti:Al_2O_3 with 30 ns pulse width or its doubled emission, the luminescence was collected from a small portion of the crystal and the signal from the detector was sent to a digital oscilloscope. The system response time was about 1 μs.

3. Structural data and absorption spectroscopy

BNN is a ferroelectric crystal having the tetragonal tungsten bronze (TTB) structure, with space group $P4bm$, cell parameters $a = 12.463$ Å and $c = 3.990$ Å and $Z = 2$ [6]. Its structure can be described as a framework of corner sharing NbO_6^{7-} octahedra, whose linking produces three different types of channels containing the A_1, A_2 and C cation sites having 15-fold, 12-fold and 9-fold oxygen coordination, respectively [8]. The A_1 sites are occupied by Ba^{2+}, the A_2 ones by Na^+, whereas the small C cavities are empty. The XRD analysis indicates that Tm^{3+} and Ho^{3+} should preferentially replace Na^+ in the A_2 sites, even if the site occupancy of the rare earth ions in BNN is still an open question [5]. In any case, the incorporation of rare earth ions into

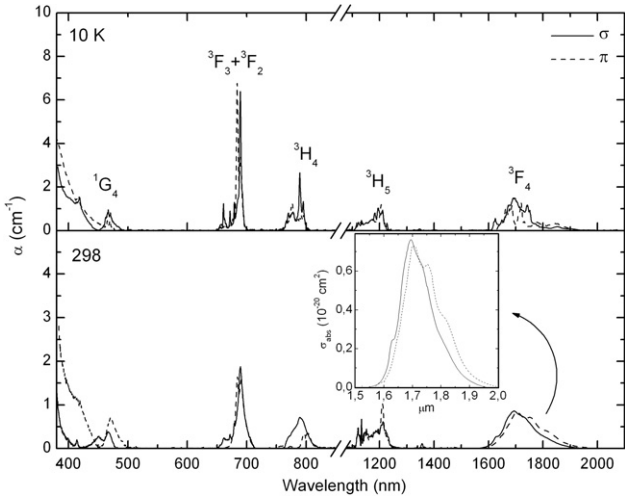

Figure 1. 10 and 298 K polarized absorption spectra of Tm:BNN.

Table 1. Line wavelengths observed in the 10 K absorption spectra of Tm:BNN and Ho:BNN.

	Assignment	Wavelength (nm)
Tm:BNN	$^3F_4$	1853, 1775, 1743, 1720, 1692, 1674,1660, 1648, 1625
	$^3H_5$	1227, 1208, 1194, 1184, 1176, 1165, 1148, 1134, 1122, 1101
	$^3H_4$	795.4, 789.6, 777.0, 767.0, 761.1
	$^3F_2 + {}^3F_3$	692.6, 689.0, 690.2, 688.8, 684.0, 679.3, 676.4, 672.2, 665.4, 663.0, 661.0, 657.2, 655.1
	$^1G_4$	483.8, 470.6, 469.0, 467.0, 462.6, 458.6
Ho:BNN	$^5I_7$	1938, 1928, 1921, 1917, 1893, 1878, 1875, 1872, 1869
	$^5I_6$	1147, 1140, 1136, 1131, 1127, 1124, 1121
	$^5I_5$	881.2
	$^5F_5$	648.6, 645.4, 642.2, 641.1, 640.5, 638.2
	$^5S_2 + {}^5F_4$	541.4, 540.0, 538.2, 537.4, 535.8, 534.8, 533.3
	$^5F_3$	486.1, 485.4, 484.8, 484.0, 482.0
	$^5F_2 + {}^3K_8$	473.1, 471.6, 469.0, 467.2, 465.2, 463.8
	$^5G_6$	453.6, 452.6, 451.0, 450.0, 448.1, 446.9, 445.8
	$^3G_5$	417.0, 415.4
	$^5G_4 + {}^3K_7$	387.4, 386.5, 386.0, 384.8, 381.6
	$^5G_5$	362.4, 361.0, 360.2, 359.2

this lattice requires charge compensation, and this implies the formation of a number of non-equivalent optical centres. Moreover, the BNN structure is affected by a quasicommensurate structural modulation generated by the cooperative tilting of the NbO_6^{7-} octahedra. This implies a certain degree of disorder in the orientation and/or shape of the coordination polyhedra, and then in the crystal field around the active ions. As a result, we have to expect an inhomogeneous broadening of the optical features even in the low temperature spectra.

This broadening effect is clearly visible in the LT and RT absorption spectra of the 7% Tm:BNN, reported in figure 1. They are composed of multiplets corresponding to transitions from the $^3H_6$ ground state to the excited states of Tm^{3+} ($4f^{10}$ electronic configuration). They have been assigned on the basis of the energy level diagram reported in the literature [4]. The line wavelengths observed in the 10 K spectra are reported in table 1. Thanks to its broadness the $^3F_4 \leftarrow {}^3H_6$ transition, having maximum absorption of 0.7 cm^{-1} at 1790 nm and FWHM

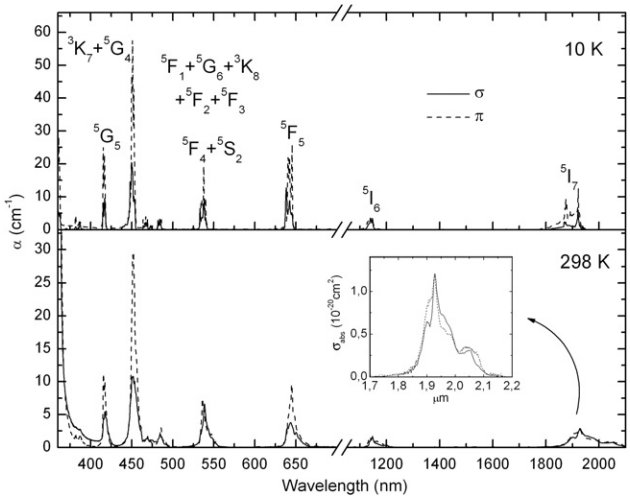

Figure 2. 10 and 298 K absorption spectra of Ho:BNN.

of 25 nm in the σ polarization, can be advantageously exploited in laser applications to match the wavelength of the pumping diode even in the presence of some thermal drift. Its absorption cross section, shown in the inset of figure 1 has a maximum value of $\approx 0.35 \times 10^{-20}$ cm^2 in both polarizations at about 1700 nm. These values are comparable with other oxide crystals doped with Tm^{3+} [3].

In figure 2 we present the absorption spectra of Ho:BNN (7% sample). As before, the transitions arising from the $^5I_8$ ground state have been assigned according to the literature [4] and their wavelengths are reported in table 1. The $^5I_5 \leftarrow {}^5I_8$ and $^5I_4 \leftarrow {}^5I_8$ transitions located in the diode pumping region (not shown in figure 2) are extremely weak and nearly undetectable, therefore not suitable for practical purposes. In the inset of figure 2 we report the absorption cross-section of the $^5I_7 \leftarrow {}^5I_8$ transition, that is involved in the $Tm^{3+} \rightarrow Ho^{3+}$ energy transfer mechanism, whose efficiency depends on the overlap between the donor emission and the acceptor absorption. In the present case the absorption cross-section peak value, 0.6×10^{-20} cm^2 at 1927 nm (slightly higher than in other Ho^{3+}-based laser crystals [3]) and the significant broadness of the band (FWHM ~ 210 cm^{-1}), constitute favourable conditions for the realization of efficient energy transfer processes.

4. Luminescence spectroscopy and decay kinetics

Both Tm^{3+} and Ho^{3+} exhibit a number of emission features in the visible and NIR region. As mentioned before, we are mainly interested in the development of a tunable laser source around 2 μm, then we have focused our attention on the transitions occurring in this region. Moreover, we have extended the investigation to the green $^5S_2 \rightarrow {}^5I_8$ transition of Ho^{3+}, which is of practical interest for a number of applications such as data storage and display applications.

4.1. $(Ho^{3+})^5S_2 \rightarrow {}^5I_8$ transition

The polarized $^5S_2 \rightarrow {}^5I_8$ emission of 7% Ho:BNN has been measured after Ar^+ laser excitation at 488 nm, as shown in figure 3. The LT spectra show at least five broad peaks in the 540–560 region, which merge into broadbands ranging from 530 to 570 nm as the temperature increases. The 298 K decay profiles of both diluted (1%) and concentrated (7%) crystals have

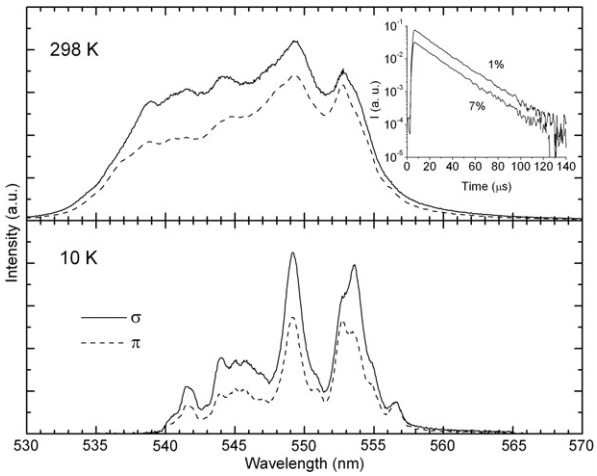

Figure 3. 10 and 298 K polarized emission of Ho:BNN in the green region ($^5S_2 \rightarrow {}^5I_8$ transition). Excitation wavelength: 488 nm. The room temperature decay profile of the luminescence is shown in the inset for two different concentrations.

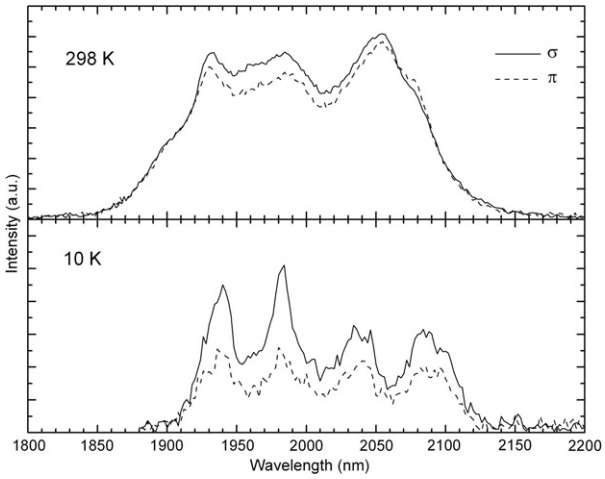

Figure 4. 10 and 298 K polarized emission of Ho:BNN in the 2 μm region. Excitation wavelength: 488 nm.

been measured with excitation at 452 nm, in correspondence with the $^5G_6$ level. They are shown in the inset of figure 3. They are single exponential with similar decay times (17.9 ± 0.3 and 17.4 ± 0.5 μs for the 1 and 7% samples respectively). The main quenching mechanisms for this transition are the multiphonon relaxation, since the energy gap between the $^5S_2$ and the next lower-lying $^5F_5$ levels, of about 2800 cm^{-1}, can be bridged by only four phonons (the highest phonon energy of the host is about 650 cm^{-1}) [5], and some cross relaxations, in particular the $(^5S_2, {}^5I_8) \rightarrow (^5I_4, {}^5I_7)$ resonant process [9].

4.2. $(Ho^{3+})^5I_7 \rightarrow {}^5I_8$ *transition*

The LT $^5I_7 \rightarrow {}^5I_8$ luminescence spectrum of the 7% Ho:BNN, shown in figure 4 presents four main broad components peaking at 1940, 1984, 2035 and 2085 nm. The broadening

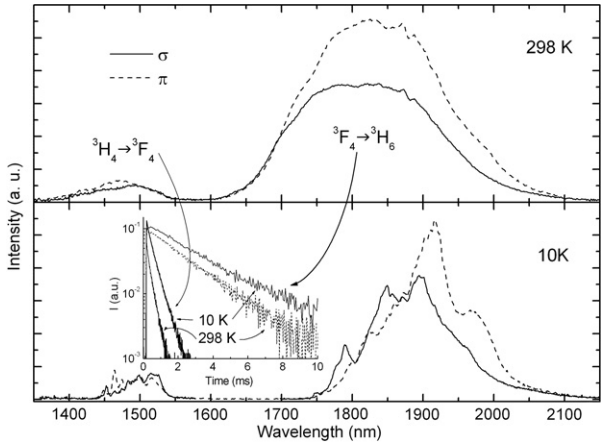

Figure 5. 10 and 298 K polarized emission of Tm:BNN in the 2 μm region. Excitation wavelength: 790 nm. The RT decay profiles of the luminescence are shown in the inset.

is more evident at RT, where the transition gives rise to a broad band system ranging from 1.8 up to 2.2 μm with three distinct main bands at 1930, 1985 and 2050 nm. The energy gap between the $^5I_7$ and $^5I_8$ levels is about 5200 cm^{-1} and needs at least eight phonons to be bridged. As a consequence, the multiphonon relaxation should be quite ineffective, in agreement with the relatively high value of the $^5I_7$ decay time of the 1% sample, 4.47 ± 0.08 at LT and 4.28 ± 0.13 ms at RT, a typical value for oxide crystals [3]. From the luminescence spectra and the decay time, we estimated the emission cross-sections by means of the β–τ method [10]. The peak values are found at 1930 (0.45×10^{-20} cm^2), 1985 (0.50×10^{-20} cm^2) and 2050 nm (0.65×10^{-20} cm^2). These values are relatively low in comparison with those reported for the 2 μm emission of Ho^{3+} in other laser hosts [3]. On the other hand, the large bandwidth suggests that this material is a promising active medium for wide-tunability and/or very short pulsed solid-state lasers.

4.3. $(Tm^{3+})^3F_4 \rightarrow {}^3H_6$

Figure 5 shows the polarized emission of the 7% Tm:BNN crystal in the 1.3–2.2 μm region. Two band systems are present. The most intense range is from 1600 up to 2200 nm and it is assigned to the $^3F_4 \rightarrow {}^3H_6$ transition whereas the weaker one, centred at about 1500 nm, is ascribed to the $^3H_4 \rightarrow {}^3F_4$ transition. At RT the main emission system consists of a single and structureless broadband with maximum emission at 1870 nm in the ($E \perp c$) polarization. At 10 K the band loses its hot components, its maximum moves towards lower energies ($\sim$1900 nm) and some weak Stark components become evident in both polarizations. We have measured the 298 K decay curves of the emissions from the $^3F_4$ and $^3H_4$ states upon excitation into the $^3H_4$ one at 790 nm. The decay profile of $^3F_4$ is single exponential, as shown in the inset of figure 5. In this case the multiphonon relaxation to the$^3H_6$ ground state is expected to be inefficient, since the energy gap between the two levels is about 5400 cm^{-1} and requires about eight phonons to be bridged. Moreover, the decay from $^3F_4$ is not usually affected by non-linear processes at low doping levels [11]. The fit of the decay curve of the 7% sample yields a decay time of 2.80 ± 0.08 ms at LT and 2.19 ± 0.04 ms at RT. The emission decay from $^3H_4$, also reported in the inset of figure 5, is not exponential. Several processes are involved in the non-radiative depopulation of this level. In the first place, the ($^3H_4$, $^3H_6$) $\rightarrow$ ($^3F_4$, $^3F_4$) cross

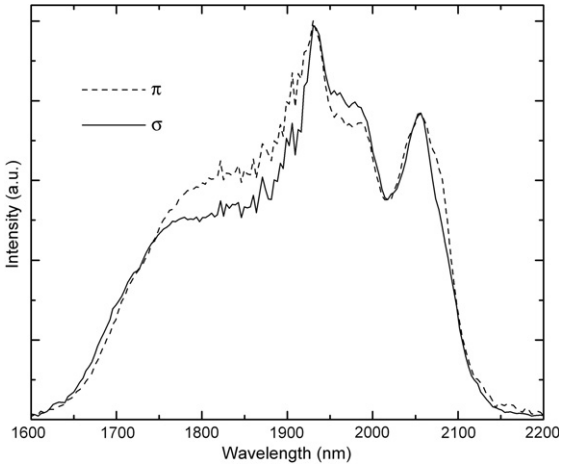

Figure 6. Room temperature polarized emission of the Tm–Ho co-doped crystal. Excitation wavelength: 790 nm.

relaxation process is important, but the multiphonon relaxation can also be important, since the gap between $^3H_4$ and the lower-lying $^3H_5$ state is about 3500 cm^{-1} and can be bridged by five high energy phonons. Moreover, reabsorption processes can also play a role in depopulating the $^3H_4$ state [12]. In the absence of a suitable model, the averaged decay times can be estimated using the integral method [13]:

$$\tau_{av} = \frac{\int I(t) \cdot t \, dt}{\int I(t) \, dt} \tag{1}$$

where $I(t)$ is the emission intensity at time t. By applying this formula to the decay profile of the emission from the $^3H_4$ state we have determined its decay time, 273 μs. Using the experimental value of the emission decay from $^3H_4$, we estimated the emission cross sections, obtaining a peak of 0.63×10^{-20} cm^2 at 1870 nm for the ($E \perp c$) polarization. This value is slightly higher than that found in other oxide hosts and comparable with that observed in $YAlO_3$ [3], with the advantage of a broader emission profile.

4.4. Tm^{3+}, Ho^{3+} co-doped crystal

The RT luminescence spectrum of the Tm, Ho co-doped crystal, shown in figure 6, is composed of the $^3F_4 \rightarrow {}^3H_6$ (Tm^{3+}) and $^5I_7 \rightarrow {}^5I_8$ (Ho^{3+}) transitions. At variance with the spectra-ordered crystals like YAG and $YAlO_3$ [3], constituted of distinct emission manifolds, in this case the optical features merge into a single broadband as a consequence of the presence of non-equivalent centres and of the structure modulation. This band presents three components: the first one extends from 1600 up to approximately 1800 nm and is assigned to the $^3F_4 \rightarrow {}^3H_6$ emission of Tm^{3+}. In the 1850–1900 nm region this band strongly overlaps the $^5I_7 \rightarrow {}^5I_8$ transition of Ho^{3+}, well identifiable by the peaks at 1930 nm (with the nearby component at 1985 nm) and 2050 nm present in the spectrum of figure 4. The decay profile of this last emission is single exponential, and the fit yields a value of 4.75 ± 0.06 ms at LT and 3.71 ± 0.04 ms at RT, close to that of the singly doped crystal. The decrease of the decay time with the temperature may be related to the increase of the Ho–Tm back transfer (see next section).

Table 2. Experimental and calculated oscillator strengths (P) of Tm:BNN.

Transition	Barycentre (cm^{-1})	P_{exp} (10^{-6})	P_{calc} (10^{-6})
$^3F_4 \leftarrow {}^3H_6$	5 786	2.52	2.51
$^3H_5 \leftarrow {}^3H_6$	8 485	1.31	1.45
$^3H_4 \leftarrow {}^3H_6$	12 606	1.42	1.37
$^3F_3 + {}^3F_2 \leftarrow {}^3H_6$	14 540	3.66	3.55
$\Omega_2 = 0.11 \times 10^{-20}$ cm^2, $\Omega_4 = 2.58 \times 10^{-20}$ cm^2, $\Omega_6 = 0.27 \times 10^{-20}$ cm^2			
RMS $= 1.88 \times 10^{-7}$; %RMS $= 8.4$			

Table 3. Experimental and calculated oscillator strengths (P) of Ho:BNN.

Transition	Barycentre (cm^{-1})	P_{exp} (10^{-6})	P_{calc} (10^{-6})
$^5I_7 \leftarrow {}^5I_8$	5 118	0.92	1.13
$^5I_6 \leftarrow {}^5I_8$	8 631	0.97	0.76
$^5F_5 \leftarrow {}^5I_8$	15 468	3.81	4.02
$^5F_4 + {}^5S_2 \leftarrow {}^5I_8$	18 518	4.86	3.82
$^5G_6 + {}^5F_1 + {}^5F_2 + {}^3K_8 + {}^5F_2 \leftarrow {}^5I_8$	21 891	20.5	20.5
$^5G_5 + {}^3G_5 \leftarrow {}^5I_8$	23 910	5.97	6.13
$\Omega_2 = 1.67 \times 10^{-20}$ cm^2, $\Omega_4 = 2.86 \times 10^{-20}$ cm^2, $\Omega_6 = 0.58 \times 10^{-20}$ cm^2			
RMS $= 6.45 \times 10^{-7}$; %RMS $= 10.5$			

5. Judd–Ofelt analysis and $Tm^{3+} \rightarrow Ho^{3+}$ energy transfer

The RT absorption spectra have been analysed in the framework of the Judd–Ofelt theory [14, 15]. The experimental oscillator strengths were reliably determined and fitted on the basis of the Judd–Ofelt parametrization scheme after subtraction of the magnetic dipole contributions for the $^5I_7 \leftarrow {}^5I_8$ (Ho^{3+}), $^3K_8 \leftarrow {}^5I_8$ (Ho^{3+}), $^3K_7 \leftarrow {}^5I_8$ (Ho^{3+}) and $^3H_5 \leftarrow {}^3H_6$ (Tm^{3+}) transitions. In the case of Tm:BNN we have excluded the $^1G_4 \leftarrow {}^3H_6$ band from the analysis. This because the calculations carried out including this transition were unreliable, probably as a consequence of the fact that, being located in proximity of the absorption edge of the host, it can borrow part of its intensity from the niobate charge transfer band. The reduced matrix elements reported by Kaminskii [4] were used. The mean value of the refractive index of BNN was employed ($n = 2.33$). The measured and calculated oscillator strengths, the intensity parameters and the root mean square deviation (rms) are reported in tables 2 and 3. The calculated spontaneous emission probabilities, the radiative branching ratios and the radiative lifetimes were estimated using the calculated intensity parameters and correcting for the refractive index. They are reported in tables 4 and 5. From these tables we observe that the $^3F_4 \rightarrow {}^3H_6$ (Tm^{3+}) decay time is in substantial agreement with the calculated value (2.4 ms) if the intrinsic uncertainty of the Judd–Ofelt approach ($\pm 20\%$) is considered. In this case, instead of the transition originating from the $^3H_4$ level, the multiphonon relaxation plays an important role and the measured decay time is shorter than the calculated lifetime, 802 μs. The same consideration applies to the $^5S_2 \rightarrow {}^5I_8$ (Ho^{3+}) transition, where the calculated radiative lifetime is considerably longer than the measured one. The $^5I_7 \rightarrow {}^5I_8$ (Ho^{3+}) transition shows a measured decay time shorter than the calculated radiative lifetime, about 8.3 ms. This behaviour has already been observed for other crystals [9] and indicates that non-radiative processes take place in competition with the emission transitions.

As mentioned before, the $Tm^{3+} \rightarrow Ho^{3+}$ energy transfer in BNN has been dealt with in a previous paper [5]. Nevertheless, it is interesting to briefly revisit the already presented

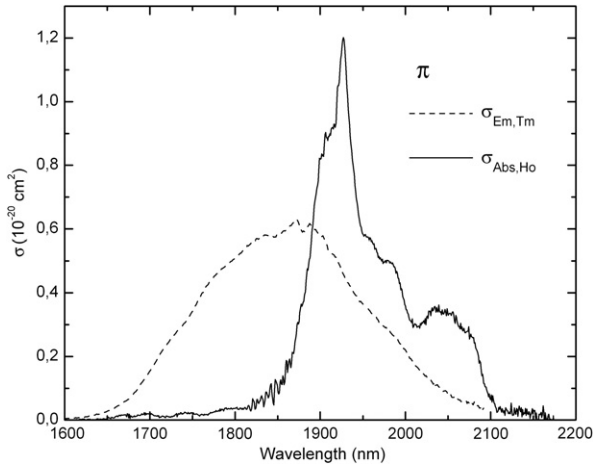

Figure 7. π polarized cross sections of the $^3F_4 \rightarrow {}^3H_6$ emission Tm:BNN and of the $^5I_7 \leftarrow {}^5I_8$ absorption of Ho:BNN.

Table 4. Calculated spontaneous emission probabilities (A), radiative branching ratios (β), radiative (τ_R) lifetimes of Tm:BNN at room temperature.

Initial state	Final state	A (s^{-1})	β	τ_R (μs)
$^1G_4$	$^3F_2 + {}^3F_3$	192	0.05	284
	$^3H_4$	188	0.05	
	$^3H_5$	709	0.20	
	$^3F_4$	301	0.09	
	$^3H_6$	2125	0.60	
$^3H_4$	$^3H_5$	114	0.09	802
	$^3F_4$	197.15	0.16	
	$^3H_6$	935	0.75	
$^3H_5$	$^3F_4$	4	0.01	1730
	$^3H_6$	573	0.99	
$^3F_4$	$^3H_6$	422	1	2371

results in order to give a complete picture of the potentialities of the investigated material. Since we are interested in obtaining an efficient laser crystal for the 2 μm region, we have focused our attention on the $^3F_4$ (Tm^{3+}) $\rightarrow$ $^5I_7$ (Ho^{3+}) energy transfer. The efficiency of this process can be estimated by means of an energy transfer parameter defined in the Förster–Dexter theory [16, 17]. On this basis we have calculated the coefficient for the Tm–Ho direct transfer, $c_{Tm\rightarrow Ho} = 36.5 \times 10^{-40}$ $cm^6\,s^{-1}$ and that of the inverse process (back transfer) $c_{Ho\rightarrow Tm} = 4.1 \times 10^{-40}$ $cm^6\,s^{-1}$. From the comparison with analogous materials (see the table reported in [5]), we can say that the direct transfer coefficient as well as its ratio with the back transfer coefficient have high values, and these are very favourable conditions for achieving stimulated emission at 2 μm. We point out that the value of the direct transfer coefficient is related to that of the overlap integral between the emission profile of the donor (Tm^{3+}) and the absorption profile of the acceptor (Ho^{3+}). As shown in figure 7, this integral strongly depends on the broadness of the involved bands and thus on the disorder degree of the lattice and of the crystal field around the optical centres.

Table 5. Calculated spontaneous emission probabilities (A), radiative branching ratios (β), radiative (τ_R) lifetimes of Ho:BNN at room temperature.

Initial state	Final state	A (s^{-1})	β	τ_R (μs)
$^5F_4$	$^5S_2$	0	0	92
	$^5F_5$	19.3	0.002	
	$^5I_4$	35.1	0.003	
	$^5I_5$	298.7	0.027	
	$^5I_6$	930.5	0.085	
	$^5I_7$	1.62×10^3	0.149	
	$^5I_8$	8.00×10^3	0.734	
$^5S_2$	$^5F_5$	1.8	0	303
	$^5I_4$	73.5	0.022	
	$^5I_5$	59.4	0.018	
	$^5I_6$	290.1	0.088	
	$^5I_7$	1.16×10^3	0.353	
	$^5I_8$	1.71×10^3	0.518	
$^5F_5$	$^5I_4$	0.2	0	145
	$^5I_5$	14.0	0.002	
	$^5I_6$	196.3	0.029	
	$^5I_7$	1.28×10^3	0.185	
	$^5I_8$	5.40×10^3	0.784	
$^5I_4$	$^5I_5$	8.6	0.066	7710
	$^5I_6$	49.7	0.383	
	$^5I_7$	59.7	0.461	
	$^5I_8$	11.7	0.090	
$^5I_5$	$^5I_6$	13.4	0.056	4147
	$^5I_7$	120.5	0.500	
	$^5I_8$	107.2	0.445	
$^5I_6$	$^5I_7$	33.6	0.111	3313
	$^5I_8$	268.2	0.889	
$^5I_7$	$^5I_8$	120.9	1	8275

6. Conclusions

The 10 and 298 K absorption and emission properties of the Ho^{3+} and Tm^{3+} ions singly doped in BNN host crystals have been studied. The observed features are strongly broadened even at LT in consequence of the structural modulation and of the presence of different active ions arising from the charge compensation mechanisms connected to the doping processes. This make these materials interesting candidates for diode pumped and tunable solid-state laser operation. The room temperature absorption spectra have been analysed in the framework of the Judd–Ofelt approach, and the obtained intensity parameters are consistent with those reported for analogous materials [4]. The calculated radiative lifetimes have been compared with the decay times obtained from pulsed light measurements in order to estimate the efficiency of the non-radiative processes. We have then focused attention on the emission transitions that are of technological interest, in particular for laser applications in the 2 μm region. The possible sources of non-radiative deactivation of the main emitting levels have been discussed and some information about the $Tm^{3+} \rightarrow Ho^{3+}$ energy transfer has been provided. In conclusion, we think that BNN has, in principle, considerable device potentialities. For the moment, problems

in obtaining good quality single crystals of suitable size constitute the main hindrance to its technological development.

Acknowledgment

This work has been carried out with the financial contribution of the Italian Ministry for the University and Scientific Research (Project PRIN 2005).

References

[1] Sudesh V and Piper J 2000 *IEEE J. Quantum Electron.* **36** 879
[2] Sudesh V and Goldys E M 2000 *J. Opt. Soc. Am.* B **17** 1068
[3] Payne S, Chase L L, Smith L K, Kway W L and Krupke W F 1992 *IEEE J. Quantum Electron.* **36** 2619
[4] Kaminskii A A 1996 *Crystalline Lasers: Physical Processes and Operating Schemes* (New York: CRC Press)
[5] Bigotta S, Toncelli A, Tonelli M, Cavalli E and Bovero E 2007 *Opt. Mater.* **30** 129
[6] Cavalli E, Calestani G, Bovero E, Belletti A and Migliori A 2004 *J. Phys.: Condens. Matter* **16** 729
[7] Bigotta S, Gorini G, Toncelli A, Tonelli M, Cavalli E and Bovero E 2006 *Opt. Mater.* **28** 395
[8] Neurgaonkar R R and Cory W K 1986 *J. Opt. Soc. Am.* B **3** 274
[9] Malinowski M, Piramidowicz R, Frukacz Z, Chadeyron G, Mahiou R and Joubert M F 1999 *Opt. Mater.* **12** 409
[10] Aull B F and Jenssen H P 1982 *IEEE J. Quantum Electron.* **18** 925
[11] Sokólska I I, Ryba-Romanowski W, Golab S, Baba M, Swirkowicz M and Lukasiewicz T 2000 *J. Phys. Chem. Solids* **61** 1573
[12] Xueyuan C and Zundu L 1997 *J. Phys.: Condens. Matter* **9** 7981
[13] Shionoya S and Yen W M (ed) 1999 *Phosphor Handbook* (Boca Raton, FL: CRC Press) p 104
[14] Judd B R 1962 *Phys. Rev.* **127** 750
[15] Ofelt G S 1962 *J. Chem. Phys.* **37** 511
[16] Förster T 1948 *Ann. Phys.* **2** 55
[17] Dexter D L 1953 *J. Chem. Phys.* **21** 836